Noname manuscript No.
(will be inserted by the editor)

Parameter-varying Modeling and Nonlinear Model Predictive Control with Disturbance Prediction for Spar-Type Floating Offshore Wind Turbines

Yuga Okada · Ken Haneda · Toshiki Chujo · Toshiyuki Ohtsuka

Received: 19 March 2020 / Accepted: 27 September 2021

Abstract This paper proposes novel methods for the modeling and control of spar-type floating offshore wind turbines (FOWTs) by focusing on the dependency of the equilibrium and perturbed dynamics on the rotor azimuth angle. In addition, three new reduced models for controller design are derived using trajectory linearization by accounting for the dependency of the equilibrium on the azimuth angle. A thorough simulation study shows that the proposed models reproduce the important dynamic characteristics of FOWTs more accurately than the conventional models. Then, nonlinear model predictive controllers (NMPCs) minimizing the nonquadratic cost functions are developed for the proposed models, which include nonlinear terms for the rotor azimuth angle. These NMPCs suppress the variation in the forces applied to the blades better than the conventional linear MPCs while maintaining a low computational cost. The best NMPC for the models is one that accounts for the dependency of both the equilibrium and perturbed dynamics on the rotor azimuth angle. This NMPC suppresses the platform yaw and forces added on the blades. The performance of such an NMPC can be further improved by using the inflow wind disturbance data predicted using a light detection and ranging wind sensor.

Keywords Predictive control · Linearization techniques · Floating offshore wind turbine

This work was partly supported by JSPS KAKENHI Grant Number 15H02257.

Yuga Okada
Department of Systems Science, Graduate School of Informatics, Kyoto University,
Yoshida-honmachi, Sakyoku, Kyoto 606-8501, Japan
E-mail: okada.yuga.82s@kyoto-u.jp

Ken Haneda
Offshore Advanced Technology Department, National Maritime Research Institute,
Mitaka 181-0004, Japan
E-mail: haneda@mpat.go.jp

Toshiki Chujo
Offshore Advanced Technology Department, National Maritime Research Institute,
Mitaka 181-0004, Japan
E-mail: chujo@mpat.go.jp

Toshiyuki Ohtsuka
Department of Systems Science, Graduate School of Informatics, Kyoto University,
Yoshida-honmachi, Sakyoku, Kyoto 606-8501, Japan
E-mail: ohtsuka@i.kyoto-u.ac.jp

1 Introduction

Offshore wind energy has been receiving much attention because of being a renewable source, and thus, contributes to addressing the world's energy problem. According to the 2016 Offshore Wind Energy Resource Assessment for the United States [1], the offshore wind energy potential in the United States is approximately two times the electricity used in the country in 2014. Offshore wind turbines have been practically applied, and the installed offshore wind power capacity has grown remarkably [2]. Among the various offshore wind turbines, floating offshore wind turbines (FOWTs) especially exhibit considerable potential for power generation [1]. Offshore wind turbines are mounted on bottom-fixed foundations, whereas FOWTs are mounted on floating platforms. Thus, FOWTs enable power generation in deeper waters than bottom-fixed turbines.

To optimize the generated power, active control is used in operating FOWTs. There are several regions of operation to be considered in power optimization, as shown in Fig. 1, and the goal of power optimization

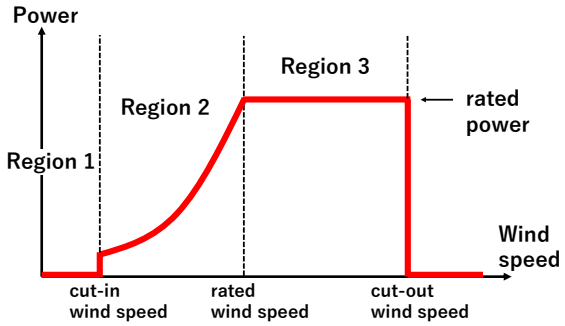

Fig. 1 Operating regions of FOWT

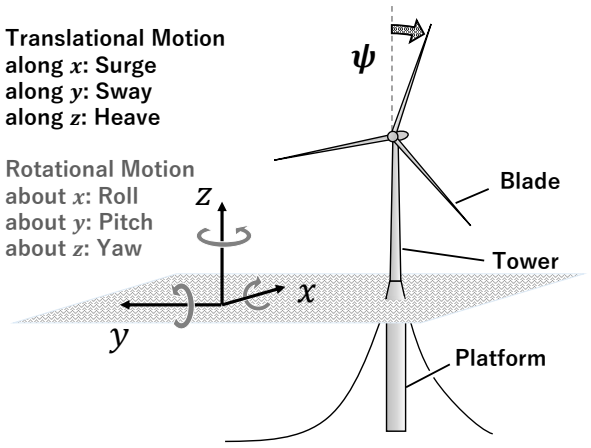

Fig. 2 Configuration of FOWT

depends on the region [3]. If the actual wind speed is below the rated wind speed (Region 2), the goal is to maximize the generated power. If it is above the rated wind speed (Region 3), the goal is to maintain the rated power. This is because the rotor rotation at an excessive speed can induce malfunctions in the wind turbine. Blade-pitch control is commonly used to regulate the rotor speed, and its control input is the blade-pitch angle, which is defined as the attack angle of the rotor blade relative to the rotor surface.

The most basic controller used in blade-pitch control is the gain-scheduled PI (GSPI) controller [4]. This controller aims to regulate the rotor speed by feeding back the difference between the measured and rated rotor speeds to the blade-pitch angle. Thus, FOWTs are treated as single-input single-output systems, where the input is the collective blade-pitch (CBP) angle. This means that the GSPI controller does not consider variables other than the rotor speed, such as the FOWT attitude and structural loads. Consequently, this controller induces negative damping in FOWTs [5], which refers to an increase in the attitude oscillations due to the resonance between the blade-pitch controller and the platform pitch mode with low natural frequencies. In FOWTs, oscillations in the platform attitude can cause serious accidents and structural fatigue damages [6]. Thus, it is important to regulate the attitude and structural loads to reduce the malfunction risk.

These several control objectives have motivated researchers to model and control FOWTs using various methods [7]. Some studies have treated FOWTs as multiple-input multiple-output (MIMO) systems [8–10], in which the individual blade-pitch (IBP) angles are generally used as the inputs. In contrast to CBP controllers, IBP controllers need to adjust the inputs in accordance with the rotor azimuth angle ψ, which is the angle between the vertical line and rotor blade, as shown in Fig. 2. For this reason, IBP controllers are designed to account for the dependency of the dynamics on ψ. This dependency is an inherent characteristic of wind turbines caused by the rotating blades.

MIMO models for FOWTs can be categorized as linear [8, 9] or nonlinear [10]. As the FOWT dynamics strongly depend on ψ, linearization is performed at each discretized point with respect to ψ, such as every 10 degrees of ψ. For this reason, the coefficient matrices in the linearized model depend on ψ. That is, the state-space representation is periodic in ψ with a period of 2π. For the controller design, the dependency on ψ is removed from the state-space representation by using the averaging operation [8] or multiblade coordinate (MBC) transformation [9, 11].

Namik et al. [8] used linear models to design linear quadratic regulators (LQRs) for CBP and IBP, focusing on regulating the rotor speed and platform pitch. As these LQRs do not consider load effects, they increase the load variation on the blades and tower. Chaaban and Fritzen [9] considered the effects of loads in addition to those of the rotor speed and platform attitude by using linearization and linear model predictive control (LMPC) for IBP. Raach et al. [10] proposed the use of a nonlinear reduced model and a nonlinear model predictive control (NMPC) for IBP. This nonlinear model was found to be accurate and the controller performance was improved. However, it was computationally expensive because the nonlinear reduced model considers interactions among subsystems: the aerodynamics, hydrodynamics, servo-elastics, and mooring line dynamics. The mean time for solving the optimization problem is 1.3 s while the sampling period is 0.2 s; thus, real-time implementation is difficult.

Kane [12] applied machine learning control (MLC) for IBP and achieved better performance than a baseline PID controller. In MLC, the control logic architecture and parameters are learned through trials on a detailed simulator for cost evaluation. However, MLC learning on a cloud computer takes three days, which is not suitable for practical controller design involving

iterative tuning of the cost and specifications. In contrast, Sarkar et al. [13] proposed a simple IBP controller by combining a linear quadratic controller with an integral action to reduce the aerodynamic loads. Moreover, Bagherieh et al. [14], Navalkar et al. [15], Zhao and Nagamune [16], Zhang et al. [17], and Yu et al. [18] applied sophisticated techniques such as input/output feedback linearization, $\mathcal{H}_\infty$ feedforward-feedback control, switching LPV control, sliding mode control, and adaptive control. However, they used linearized models removing the dependency on ψ.

Although high-performance controllers are desirable, their implementation is difficult and impractical if they are too complicated and computationally expensive. In contrast, if a simple controller is designed based on an oversimplified model not capturing the relevant dynamic characteristics, its control performance might be limited. Therefore, it is necessary to investigate the modeling and control of FOWTs in a systematic and integrated manner from the viewpoints of validity and computational cost, which has not yet been completely addressed.

This paper proposes new reduced models that are simple and capture the relevant dynamic characteristics of FOWTs for controller design. This paper particularly focuses on spar-type FOWTs used in various demonstration experiments because of its low construction costs. In the proposed models, a FOWT is linearized around a trajectory, unlike the case in the previous studies [8, 9], where a FOWT was linearized around a constant equilibrium point. As the dynamics of a FOWT strongly depend on the rotor azimuth angle ψ, it is natural to consider that the equilibrium and perturbed dynamics also depend on ψ. We then design IBP controllers on the basis of the proposed models. As the models that account for the dependency of the equilibrium on ψ include nonlinear terms for ψ, we propose to use NMPC. In this NMPC, the cost function is nonquadratic, unlike the conventional MPC, even though the state equation is linear and time-invariant. Then, we evaluate the proposed models and NMPC through a simulation study that includes a comparison with the conventional models and LMPC. We previously focused on the dependency of only the equilibrium on ψ [19]; however, in this study, we focus on the dependency of both the equilibrium and perturbed dynamics. In addition, we test the proposed controllers under wave disturbance conditions, which was not considered in our previous study. Furthermore, as the prediction of the inflow wind disturbance by using light detection and ranging (LIDAR) wind sensors has been shown to be effective for controlling FOWTs [7, 10, 15, 20, 21], we also confirm that the NMPC performance can be further improved by using the predicted data on inflow wind disturbance.

Table 1 FOWT specifications

Parameter	Value
Rating	5 MW
Rotor orientation	Upwind
Configuration	3 Blades
Rotor diameter	126 m
Hub diameter	3 m
Hub height	90 m
Draft	80.4 m
Depth	93.8 m
Water depth	150 m
Cut-in, Cut-out wind speed	3, 25 m/s
Rated wind speed	11.4 m/s
Rated rotor speed	1.267 rad/s, (12.1 rpm)
Rotor mass	3.50×10^5 kg
Tower mass	2.75×10^5 kg
Platform mass	7.17×10^6 kg

The rest of this paper is organized as follows. In Section 2, we derive the reduced FOWT models by using trajectory linearization. In Section 3, we design the controllers by using the proposed models. In Sections 4 and 5, we test the proposed models and controllers through a numerical simulation. Finally, we conclude this paper in Section 6.

2 FOWT Model

The specifications used to model a FOWT are listed in Table 1. They are defined on the basis of the specifications used for an NREL 5-MW wind turbine [4]. The turbine is mounted on a spar platform, as shown in Fig. 2, which comprises a single vertical cylinder and has been used in various demonstration experiments, such as in Norway [27] and Japan [28], because of its low construction cost.

A full-dynamics model of the FOWT is reproduced using FAST v7 [22], which was developed by the National Renewable Energy Laboratory (NREL). FAST is the standard software used for analyzing the complete dynamics of wind turbines. Although a recent version FAST v8 is available, FAST v7 is used in this study because of its flexibility in linearization and coordination with the external software. FAST v7 is validated through comparisons with the data obtained from scale testing [23–25] and field measurements [26]. Thus, we regard the FAST full model as an accurate model for our FOWT.

Although the FAST full model is accurate, it is too complicated to be used for controller design. Reduced models in the form of state-space representations are

Table 2 Linearization outputs

y_1	surge translational displacement of platform	[m]
y_2	roll rotational displacement of platform	[deg]
y_3	pitch rotational displacement of platform	[deg]
y_4	yaw rotational displacement of platform	[deg]
y_5	rotor speed	[rad/s]
y_6	blade1 out-of-plane root bending moment	[kNm]
y_7	blade2 out-of-plane root bending moment	[kNm]
y_8	blade3 out-of-plane root bending moment	[kNm]

essential for modern controller design for MIMO systems. In particular, a reduced model is crucial for the real-time implementation of NMPC because the future response of the model needs to be computed iteratively for optimizing the control input within the sampling interval.

In this paper, we derive reduced models for controller design by using the capability of FAST to extract linearized representations of the FAST full model. The FAST full model is numerically linearized about a given operating point to generate matrices in the state-space representation depending on the rotor azimuth angle ψ. Then, we derive five different models for different treatments of the operating point and periodicity in the rotor azimuth angle ψ, as discussed below. In particular, we propose three new models by explicitly accounting for the periodic equilibrium. The state vector $\boldsymbol{x}$ for linearization is defined as $\boldsymbol{x} = \left[\boldsymbol{q}^\top \dot{\boldsymbol{q}}^\top\right]^\top$, where vector $\boldsymbol{q}$ includes the following eight degrees of freedom: surge translational displacement of the platform, roll, pitch, and yaw rotational displacements of the platform, rotor azimuth angle ψ, and first bending modes of the three blades. The input vector $\boldsymbol{u}$ is the IBP angles of the three blades. The output vector $\boldsymbol{y}$ is defined in Table 2.

2.1 Conventional linearization method around a fixed equilibrium

First, we briefly review the two models obtained using the conventional linearization method [8, 9], where the full model is linearized around the constant equilibria $\bar{\boldsymbol{x}}_{\rm op}$ and $\bar{\boldsymbol{y}}_{\rm op}$. As the FOWT dynamics change periodically depending on the rotor's azimuth angle ψ, we perform linearization for the FOWT at each ψ $(0 \le \psi < 2\pi)$. The state-space representation is then derived as

$$\begin{aligned} \Delta\dot{\boldsymbol{x}} &= A_0(\psi)\,\Delta\boldsymbol{x} + B_0(\psi)\,\Delta\boldsymbol{u} \\ \Delta\boldsymbol{y} &= C_0(\psi)\,\Delta\boldsymbol{x} + D_0(\psi)\,\Delta\boldsymbol{u}, \end{aligned} \tag{1}$$

where

$$\begin{aligned} \Delta\boldsymbol{x} &:= \boldsymbol{x} - \bar{\boldsymbol{x}}_{\rm op} \\ \Delta\boldsymbol{y} &:= \boldsymbol{y} - \bar{\boldsymbol{y}}_{\rm op} \\ \Delta\boldsymbol{u} &:= \boldsymbol{u} - \boldsymbol{u}_{\rm op}. \end{aligned}$$

Here, $\Delta\boldsymbol{x}$ is the perturbed state vector, $\Delta\boldsymbol{y}$ is the perturbed output vector, and $\Delta\boldsymbol{u}$ is the perturbed input vector from the constant operating point $\boldsymbol{u}_{\rm op}$. This state-space representation contains nonlinear terms for ψ, because some elements of the coefficient matrices in (1) include trigonometric functions of ψ, which is also an element of the state vector $\boldsymbol{x}$. We remove this dependency on ψ from the coefficient matrices for the controller design by using the same approach as that followed previously [8, 9].

2.1.1 Averaged model with a fixed equilibrium

In the first conventional model, we remove the dependency on ψ from the model given in (1) in accordance with [8]. We first average the coefficient matrices, $A_0(\psi)$, $B_0(\psi)$, $C_0(\psi)$, and $D_0(\psi)$, with respect to ψ. For example, $A_0(\psi)$ is averaged as

$$\bar{A}_0 := \frac{1}{2\pi}\int_0^{2\pi} A_0(\psi)\,d\psi,$$

where the integration is performed numerically with $\pi/18$ (10 degrees) increment in ψ. Then, we derive the state-space representation as follows:

$$\begin{aligned} \Delta\dot{\boldsymbol{x}} &= \bar{A}_0\,\Delta\boldsymbol{x} + \bar{B}_0\,\Delta\boldsymbol{u} \\ \Delta\boldsymbol{y} &= \bar{C}_0\,\Delta\boldsymbol{x} + \bar{D}_0\,\Delta\boldsymbol{u} \\ \Delta\boldsymbol{u} &= \boldsymbol{u} - \boldsymbol{u}_{\rm op} \\ \boldsymbol{x} &= \Delta\boldsymbol{x} + \bar{\boldsymbol{x}}_{\rm op} \\ \boldsymbol{y} &= \Delta\boldsymbol{y} + \bar{\boldsymbol{y}}_{\rm op}. \end{aligned} \tag{2}$$

We refer to this model (2) as the "averaged model with a fixed equilibrium (Av-F model)." It should be noted that ψ does not appear in (2).

2.1.2 MBC model with a fixed equilibrium

In the second conventional model, we remove the dependency on ψ from the model given in (1) through MBC transformation [11] in accordance with [9]. MBC transformation enables the state-space representation in rotating coordinates to be rewritten as that in nonrotating coordinates. The rotating coordinates are attached to the individual blades, whose variables are expressed in rotating coordinates. By expressing the state-space representation in nonrotating coordinates, we weaken the dependence on ψ. After the MBC transformation, the periodicities are weakened; thus, the coefficient matrices can be averaged on ψ with little loss of information. The details are given elsewhere [11].

Let q_i $(i = 1, 2, 3)$ be the variable corresponding to the ith blade and ψ be the azimuth angle of blade1.

Then, the MBC transformation $T(\psi)$ is expressed as

$$\begin{bmatrix} q_1 \\ q_2 \\ q_3 \end{bmatrix} = \begin{bmatrix} 1 & \cos\psi & \sin\psi \\ 1 & \cos\left(\psi+\frac{2}{3}\pi\right) & \sin\left(\psi+\frac{2}{3}\pi\right) \\ 1 & \cos\left(\psi+\frac{4}{3}\pi\right) & \sin\left(\psi+\frac{4}{3}\pi\right) \end{bmatrix} \begin{bmatrix} q_\mathrm{o} \\ q_\mathrm{c} \\ q_\mathrm{s} \end{bmatrix} = T(\psi)\, \boldsymbol{q}_\mathrm{nr},$$

where q_o is the collective mode, q_c is the cosine-cyclic mode, and q_s is the sine-cyclic mode. We consider that vector $\boldsymbol{q}_\mathrm{nr} = [q_\mathrm{o}\, q_\mathrm{c}\, q_\mathrm{s}]^\top$ can be expressed in nonrotating coordinates. The MBC transformation $T(\psi)$ can transform the input $\boldsymbol{u}$, which comprises only three variables for the three blades. In addition, we define MBC transformations for the state $\boldsymbol{x}$ and output $\boldsymbol{y}$, which include the variables for the FOWT parts other than the blades, as follows:

$$T_x(\psi) := \text{block-diag}\left(I_5,\, T(\psi),\, O_5,\, \frac{\partial T}{\partial \psi}(\psi)\right)$$
$$T_y(\psi) := \text{block-diag}\left(I_5,\, T(\psi)\right).$$

By applying MBC transformation to (1), we obtain

$$\begin{aligned} \Delta\dot{\boldsymbol{x}}_\mathrm{nr} &= A_\mathrm{0nr}(\psi)\,\Delta\boldsymbol{x}_\mathrm{nr} + B_\mathrm{0nr}(\psi)\,\Delta\boldsymbol{u}_\mathrm{nr} \\ \Delta\boldsymbol{y}_\mathrm{nr} &= C_\mathrm{0nr}(\psi)\,\Delta\boldsymbol{x}_\mathrm{nr} + D_\mathrm{0nr}(\psi)\,\Delta\boldsymbol{u}_\mathrm{nr}, \end{aligned} \tag{3}$$

where

$$\begin{aligned} \Delta\boldsymbol{x}_\mathrm{nr} &:= {T_x}^{-1}(\psi)\,\Delta\boldsymbol{x} = {T_x}^{-1}(\psi)\,(\boldsymbol{x}-\bar{\boldsymbol{x}}_\mathrm{op}) \\ \Delta\boldsymbol{y}_\mathrm{nr} &:= {T_y}^{-1}(\psi)\,\Delta\boldsymbol{y} = {T_y}^{-1}(\psi)\,(\boldsymbol{y}-\bar{\boldsymbol{y}}_\mathrm{op}) \\ \Delta\boldsymbol{u}_\mathrm{nr} &:= T^{-1}(\psi)\,\Delta\boldsymbol{u}. \end{aligned}$$

By averaging the coefficient matrices for $0 \le \psi < 2\pi$, the above equations can be rewritten as

$$\begin{aligned} \Delta\dot{\boldsymbol{x}}_\mathrm{nr} &= \bar{A}_\mathrm{0nr}\,\Delta\boldsymbol{x}_\mathrm{nr} + \bar{B}_\mathrm{0nr}\,\Delta\boldsymbol{u}_\mathrm{nr} \\ \Delta\boldsymbol{y}_\mathrm{nr} &= \bar{C}_\mathrm{0nr}\,\Delta\boldsymbol{x}_\mathrm{nr} + \bar{D}_\mathrm{0nr}\,\Delta\boldsymbol{u}_\mathrm{nr} \\ \Delta\boldsymbol{u}_\mathrm{nr} &= T^{-1}(\psi)\,\Delta\boldsymbol{u} \\ \boldsymbol{x} &= T_x(\psi)\,\Delta\boldsymbol{x}_\mathrm{nr} + \bar{\boldsymbol{x}}_\mathrm{op} \\ \boldsymbol{y} &= T_y(\psi)\,\Delta\boldsymbol{y}_\mathrm{nr} + \bar{\boldsymbol{y}}_\mathrm{op}, \end{aligned} \tag{4}$$

where the state equation is invariant with respect to ψ. We refer to this model (4) as the "MBC model with a fixed equilibrium (MBC-F model)." As the equilibria $\bar{\boldsymbol{x}}_\mathrm{op}$ and $\bar{\boldsymbol{y}}_\mathrm{op}$ do not depend on ψ, they do not need to be expressed in nonrotating coordinates. Thus, the equilibria $\bar{\boldsymbol{x}}_\mathrm{op}$ and $\bar{\boldsymbol{y}}_\mathrm{op}$ are added to the outputs $T_x(\psi)\,\Delta\boldsymbol{x}_\mathrm{nr}$ and $T_y(\psi)\,\Delta\boldsymbol{y}_\mathrm{nr}$ of the perturbed dynamics after MBC transformation, as shown in Fig. 3. Note that ψ appears in the coefficient matrices of $\Delta\boldsymbol{u}$, $\Delta\boldsymbol{x}_\mathrm{nr}$, and $\Delta\boldsymbol{y}_\mathrm{nr}$ in (4).

2.2 Proposed linearization method around a periodic equilibrium

Next, we propose new methods to derive three different models, where the full model is linearized around the trajectories $\boldsymbol{x}_\mathrm{op}(\psi)$ and $\boldsymbol{y}_\mathrm{op}(\psi)$ instead of the constant equilibria in the conventional method. By linearizing the full model at each ψ $(0 \le \psi < 2\pi)$ around $\boldsymbol{x}_\mathrm{op}(\psi)$ and $\boldsymbol{y}_\mathrm{op}(\psi)$, we obtain the following state-space representation:

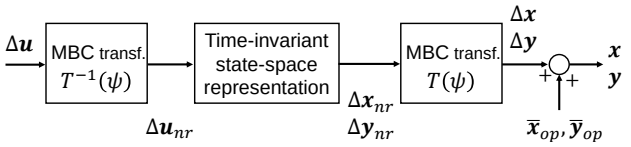

Fig. 3 Flow of MBC model with a fixed equilibrium

$$\begin{aligned} \Delta\dot{\boldsymbol{x}} &= A(\psi)\,\Delta\boldsymbol{x} + B(\psi)\,\Delta\boldsymbol{u} \\ \Delta\boldsymbol{y} &= C(\psi)\,\Delta\boldsymbol{x} + D(\psi)\,\Delta\boldsymbol{u}, \end{aligned} \tag{5}$$

where

$$\begin{aligned} \Delta\boldsymbol{x} &:= \boldsymbol{x} - \boldsymbol{x}_\mathrm{op}(\psi) \\ \Delta\boldsymbol{y} &:= \boldsymbol{y} - \boldsymbol{y}_\mathrm{op}(\psi) \\ \Delta\boldsymbol{u} &:= \boldsymbol{u} - \boldsymbol{u}_\mathrm{op}. \end{aligned} \tag{6}$$

The equilibria $\boldsymbol{x}_\mathrm{op}(\psi)$ and $\boldsymbol{y}_\mathrm{op}(\psi)$ depend on ψ in this model (5), unlike model (1). The relation between the fixed and periodic equilibria can be expressed as

$$\bar{\boldsymbol{x}}_\mathrm{op} := \frac{1}{2\pi}\int_0^{2\pi} \boldsymbol{x}_\mathrm{op}(\psi)\,d\psi$$
$$\bar{\boldsymbol{y}}_\mathrm{op} := \frac{1}{2\pi}\int_0^{2\pi} \boldsymbol{y}_\mathrm{op}(\psi)\,d\psi,$$

where the integrations are performed numerically with $\pi/18$ increment in ψ.

2.2.1 Averaged model with a periodic equilibrium

In the first proposed model, we average the coefficient matrices of model (5) ($A(\psi)$, $B(\psi)$, $C(\psi)$, and $D(\psi)$) for $0 \le \psi < 2\pi$ in the same manner as that for the Av-F model. We do not average the periodic equilibria, $\boldsymbol{x}_\mathrm{op}(\psi)$, and $\boldsymbol{y}_\mathrm{op}(\psi)$. Instead, we construct the continuous functions $\boldsymbol{x}_\mathrm{op}(\psi)$ and $\boldsymbol{y}_\mathrm{op}(\psi)$ by using second-degree trigonometric interpolations of the equilibria for $\psi = k\pi/18$ $(k = 0, \ldots, 35)$. We thereby obtain

$$\begin{aligned} \Delta\dot{\boldsymbol{x}} &= \bar{A}\,\Delta\boldsymbol{x} + \bar{B}\,\Delta\boldsymbol{u} \\ \Delta\boldsymbol{y} &= \bar{C}\,\Delta\boldsymbol{x} + \bar{D}\,\Delta\boldsymbol{u} \\ \Delta\boldsymbol{u} &= \boldsymbol{u} - \boldsymbol{u}_\mathrm{op} \\ \boldsymbol{x} &= \Delta\boldsymbol{x} + \boldsymbol{x}_\mathrm{op}(\psi) \\ \boldsymbol{y} &= \Delta\boldsymbol{y} + \boldsymbol{y}_\mathrm{op}(\psi). \end{aligned} \tag{7}$$

We refer to this model (7) as the "averaged model with a periodic equilibrium (Av-P model)." Note that ψ appears only in $\boldsymbol{x}_\mathrm{op}(\psi)$ and $\boldsymbol{y}_\mathrm{op}(\psi)$ in (7). That is, this model accounts for the dependency of the equilibria $\boldsymbol{x}_\mathrm{op}(\psi)$ and $\boldsymbol{y}_\mathrm{op}(\psi)$ on ψ but not that of the perturbed dynamics of $\Delta\boldsymbol{x}$ and $\Delta\boldsymbol{y}$ on ψ.

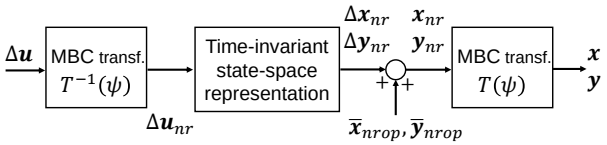

Fig. 4 Flow of MBC model with a periodic equilibrium

2.2.2 MBC model with a periodic equilibrium

In the second proposed model, by applying MBC transformations to (5), we obtain the following equations:

$$\begin{aligned}\Delta\dot{\boldsymbol{x}}_{\mathrm{nr}} &= A_{\mathrm{nr}}(\psi)\,\Delta\boldsymbol{x}_{\mathrm{nr}} + B_{\mathrm{nr}}(\psi)\,\Delta\boldsymbol{u}_{\mathrm{nr}}\\ \Delta\boldsymbol{y}_{\mathrm{nr}} &= C_{\mathrm{nr}}(\psi)\,\Delta\boldsymbol{x}_{\mathrm{nr}} + D_{\mathrm{nr}}(\psi)\,\Delta\boldsymbol{u}_{\mathrm{nr}},\end{aligned} \tag{8}$$

where

$$\begin{aligned}\Delta\boldsymbol{x}_{\mathrm{nr}} &:= {T_x}^{-1}(\psi)\,\Delta\boldsymbol{x} = {T_x}^{-1}(\psi)\,\boldsymbol{x} - \boldsymbol{x}_{\mathrm{nrop}}(\psi)\\ \Delta\boldsymbol{y}_{\mathrm{nr}} &:= {T_y}^{-1}(\psi)\,\Delta\boldsymbol{y} = {T_y}^{-1}(\psi)\,\boldsymbol{y} - \boldsymbol{y}_{\mathrm{nrop}}(\psi)\\ \Delta\boldsymbol{u}_{\mathrm{nr}} &:= T^{-1}(\psi)\,\Delta\boldsymbol{u}.\end{aligned}$$

By averaging the coefficient matrices and equilibria for $0 \le \psi < 2\pi$, we can rewrite these equations as

$$\begin{aligned}\Delta\dot{\boldsymbol{x}}_{\mathrm{nr}} &= \bar{A}_{\mathrm{nr}}\,\Delta\boldsymbol{x}_{\mathrm{nr}} + \bar{B}_{\mathrm{nr}}\,\Delta\boldsymbol{u}_{\mathrm{nr}}\\ \Delta\boldsymbol{y}_{\mathrm{nr}} &= \bar{C}_{\mathrm{nr}}\,\Delta\boldsymbol{x}_{\mathrm{nr}} + \bar{D}_{\mathrm{nr}}\,\Delta\boldsymbol{u}_{\mathrm{nr}}\\ \Delta\boldsymbol{u}_{\mathrm{nr}} &= T^{-1}(\psi)\,\Delta\boldsymbol{u}\\ \boldsymbol{x} &= T_x(\psi)\,(\Delta\boldsymbol{x}_{\mathrm{nr}} + \bar{\boldsymbol{x}}_{\mathrm{nrop}})\\ \boldsymbol{y} &= T_y(\psi)\,(\Delta\boldsymbol{y}_{\mathrm{nr}} + \bar{\boldsymbol{y}}_{\mathrm{nrop}}),\end{aligned} \tag{9}$$

where $\bar{\boldsymbol{x}}_{\mathrm{nrop}}$ and $\bar{\boldsymbol{y}}_{\mathrm{nrop}}$ are the averages of $\boldsymbol{x}_{\mathrm{nrop}}(\psi)$ and $\boldsymbol{y}_{\mathrm{nrop}}(\psi)$, respectively. We refer to this model (9) as the "MBC model with a periodic equilibrium (MBC-P model)." Note that ψ appears in the coefficient matrices of $\Delta\boldsymbol{u}$, $\Delta\boldsymbol{x}_{\mathrm{nr}}+\bar{\boldsymbol{x}}_{\mathrm{nrop}}$, and $\Delta\boldsymbol{y}_{\mathrm{nr}}+\bar{\boldsymbol{y}}_{\mathrm{nrop}}$ in (9). As the equilibria of $\boldsymbol{x}$ and $\boldsymbol{y}$ depend on ψ as $T_x(\psi)\,\bar{\boldsymbol{x}}_{\mathrm{nrop}}$ and $T_y(\psi)\,\bar{\boldsymbol{y}}_{\mathrm{nrop}}$, they also need to be expressed in nonrotating coordinates. Thus, the equilibria $\bar{\boldsymbol{x}}_{\mathrm{nrop}}$ and $\bar{\boldsymbol{y}}_{\mathrm{nrop}}$ in nonrotating coordinates are added before MBC transformation, as shown in Fig. 4, in contrast to the MBC-F model shown in Fig. 3.

2.2.3 MBC model with a periodic equilibrium including disturbance model

Finally, as the third proposed model, we derive a reduced model for the controller, which uses the predicted wind disturbance data by adding the effect of wind disturbance to the MBC-P model. We assume that the inflow wind turbulence does not evolve and that the LIDAR wind sensor exhibits the specified performance.

We define the disturbance input u_{d} [m/s] as the horizontal inflow wind speed that is perpendicular to the rotor surface. By performing linearization, we obtain the following equations:

$$\begin{aligned}\Delta\dot{\boldsymbol{x}} &= A(\psi)\,\Delta\boldsymbol{x} + B(\psi)\,\Delta\boldsymbol{u} + B_{\mathrm{d}}(\psi)\,\Delta u_{\mathrm{d}}\\ \Delta\boldsymbol{y} &= C(\psi)\,\Delta\boldsymbol{x} + D(\psi)\,\Delta\boldsymbol{u} + D_{\mathrm{d}}(\psi)\,\Delta u_{\mathrm{d}},\end{aligned}$$

where

$$\begin{aligned}\Delta\boldsymbol{x} &:= \boldsymbol{x} - \boldsymbol{x}_{\mathrm{op}}(\psi)\\ \Delta\boldsymbol{y} &:= \boldsymbol{y} - \boldsymbol{y}_{\mathrm{op}}(\psi)\\ \Delta\boldsymbol{u} &:= \boldsymbol{u} - \boldsymbol{u}_{\mathrm{op}}\\ \Delta u_{\mathrm{d}} &:= u_d - u_{\mathrm{dop}},\end{aligned}$$

and Δu_{d} is the perturbed wind disturbance from the constant operating point u_{dop}. Then, by applying MBC transformations and averaging the coefficient matrices for $0 \le \psi < 2\pi$, we can rewrite the equations as

$$\begin{aligned}\Delta\dot{\boldsymbol{x}}_{\mathrm{nr}} &= \bar{A}_{\mathrm{nr}}\,\Delta\boldsymbol{x}_{\mathrm{nr}} + \bar{B}_{\mathrm{nr}}\,\Delta\boldsymbol{u}_{\mathrm{nr}} + \bar{B}_{\mathrm{dnr}}\,\Delta u_{\mathrm{d}}\\ \Delta\boldsymbol{y}_{\mathrm{nr}} &= \bar{C}_{\mathrm{nr}}\,\Delta\boldsymbol{x}_{\mathrm{nr}} + \bar{D}_{\mathrm{nr}}\,\Delta\boldsymbol{u}_{\mathrm{nr}} + \bar{D}_{\mathrm{dnr}}\,\Delta u_{\mathrm{d}}\\ \Delta\boldsymbol{u}_{\mathrm{nr}} &= T^{-1}(\psi)\,\Delta\boldsymbol{u}\\ \boldsymbol{x} &= T_x(\psi)\,(\Delta\boldsymbol{x}_{\mathrm{nr}} + \bar{\boldsymbol{x}}_{\mathrm{nrop}})\\ \boldsymbol{y} &= T_y(\psi)\,(\Delta\boldsymbol{y}_{\mathrm{nr}} + \bar{\boldsymbol{y}}_{\mathrm{nrop}}).\end{aligned} \tag{10}$$

We refer to this model (10) as the "MBC model with a periodic equilibrium including disturbance model (MBC-P-D model)." Note that (10) is the same as (4), except for the additional linear term of Δu_{d}.

Table 3 shows the differences among the five reduced models, and Fig. 5 shows their relations. The simulation results obtained for the comparison tests focusing on these differences are presented in Section 4.

3 Controller Design

This section describes the controller design for the models presented in the previous section. As the proposed Av-P, MBC-P, and MBC-P-D models include nonlinear terms for ψ, i.e., $\boldsymbol{x}_{\mathrm{op}}(\psi)$, $\boldsymbol{y}_{\mathrm{op}}(\psi)$, $T_x(\psi)$, or $T_y(\psi)$, we propose to use NMPC for these models. They include nonlinearities only in the equations for $\boldsymbol{x}$ and $\boldsymbol{y}$, and their state equations for $\Delta\boldsymbol{x}$ or $\Delta\boldsymbol{x}_{\mathrm{nr}}$ are linear and time-invariant. To enable comparison tests to be performed under the same conditions, we use LMPC for the conventional Av-F and MBC-F models.

NMPC is a state feedback control achieved by solving an optimal control problem over a finite horizon at each time. We consider a system governed by the following state equation:

$$\dot{\boldsymbol{x}}(t) = f(\boldsymbol{x}(t), \boldsymbol{u}(t)).$$

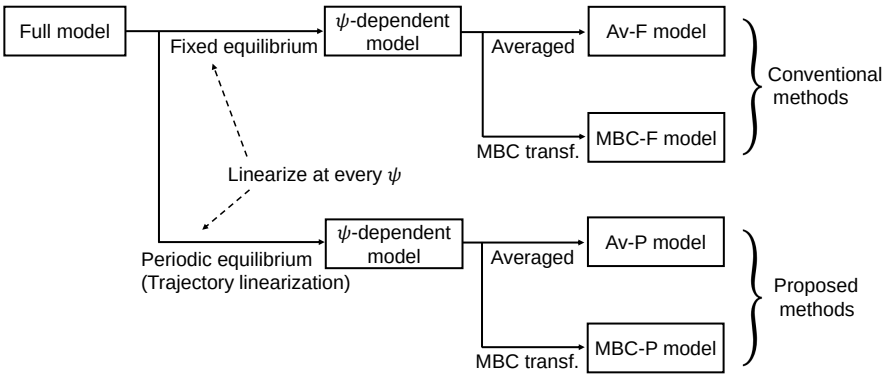

Fig. 5 Relations among Av-F, MBC-F, Av-P, and MBC-P models

Table 3 Differences among the five reduced models

Model	Av-F (2)	MBC-F (4)	Av-P (7)	MBC-P (9)	MBC-P-D (10)
State equation is linear and time-invariant.	✓	✓	✓	✓	✓
Dependency of equilibrium on ψ is considered.			✓	✓	✓
Dependency of perturbed dynamics on ψ is considered.		✓		✓	✓
Wind disturbance is considered.					✓

In NMPC, the control input at each time t is determined as follows. First, an optimal control problem is solved to minimize the cost function

$$J = \varphi\left(\boldsymbol{x}\left(t+T\right)\right) + \int_{t}^{t+T} L\left(\boldsymbol{x}\left(\tau\right), \boldsymbol{u}\left(\tau\right)\right) d\tau$$

and determine an optimal control $\boldsymbol{u}^{*}\left(\tau\right)$ $\left(t \leq \tau \leq t+T\right)$. Then, the actual input to the system is given by the initial value of the optimal control on the horizon, $\boldsymbol{u}^{*}\left(t\right)$. Consequently, the state feedback control is achieved because the optimal control depends on the current state $\boldsymbol{x}\left(t\right)$.

An important part of designing MPCs is defining the cost functions φ and L. Here, we define the cost function for each LMPC and NMPC. For the MPCs, we set the reference values to the same values of $\bar{\boldsymbol{x}}_{\mathrm{op}}$ and $\bar{\boldsymbol{y}}_{\mathrm{op}}$. Then, the control objective is to minimize the deviations $\boldsymbol{x}-\bar{\boldsymbol{x}}_{\mathrm{op}}$ and $\boldsymbol{y}-\bar{\boldsymbol{y}}_{\mathrm{op}}$. In addition, we assume that the state vector can be measured or estimated with sufficient accuracy.

3.1 LMPC based on the Av-F model

First, we define the cost function for using the Av-F model. Minimizing $\boldsymbol{x}-\bar{\boldsymbol{x}}_{\mathrm{op}}$ is equivalent to minimizing $\Delta\boldsymbol{x}$ because $\boldsymbol{x}-\bar{\boldsymbol{x}}_{\mathrm{op}} = \Delta\boldsymbol{x}$. The same is true for $\boldsymbol{y}-\bar{\boldsymbol{y}}_{\mathrm{op}}$; thus, we define the cost functions for the Av-F model as

$$\varphi = \frac{1}{2}\Delta\boldsymbol{x}^{\top} Q_x \Delta\boldsymbol{x}$$
$$L = \frac{1}{2}\left(\Delta\boldsymbol{y}^{\top} Q_y \Delta\boldsymbol{y} + \Delta\boldsymbol{u}^{\top} R \Delta\boldsymbol{u}\right),$$

where Q_x, Q_y, and R are the weighting matrices. This problem is LMPC because the model is linear and the cost functions are quadratic.

3.2 LMPC based on the MBC-F model

For the MBC-F model, minimizing $\boldsymbol{y}-\bar{\boldsymbol{y}}_{\mathrm{op}}$ corresponds to minimizing $\Delta\boldsymbol{y}_{\mathrm{nr}}$ because $\boldsymbol{y}-\bar{\boldsymbol{y}}_{\mathrm{op}} = T_y\left(\psi\right)\Delta\boldsymbol{y}_{\mathrm{nr}}$. In accordance with the previous study [9], we define the cost functions for the MBC-F model as

$$\varphi = \frac{1}{2}\Delta\boldsymbol{x}_{\mathrm{nr}}^{\top} Q_x \Delta\boldsymbol{x}_{\mathrm{nr}}$$
$$L = \frac{1}{2}\left(\Delta\boldsymbol{y}_{\mathrm{nr}}^{\top} Q_y \Delta\boldsymbol{y}_{\mathrm{nr}} + \Delta\boldsymbol{u}_{\mathrm{nr}}^{\top} R \Delta\boldsymbol{u}_{\mathrm{nr}}\right).$$

This problem is also LMPC because the model is linear and the cost functions are quadratic.

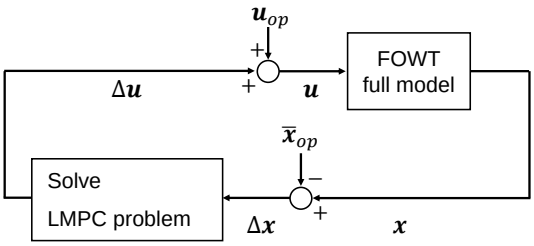

Fig. 6 Control system for LMPC based on the Av-F model

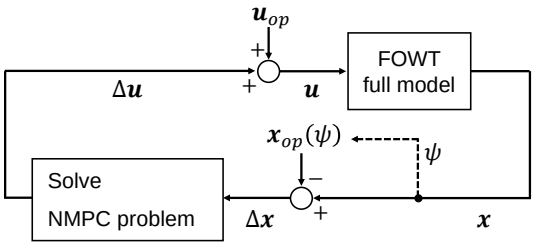

Fig. 8 Control system for NMPC based on the Av-P model

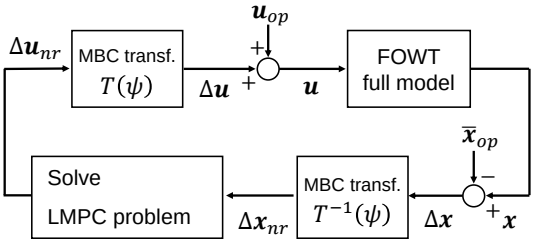

Fig. 7 Control system for LMPC based on the MBC-F model

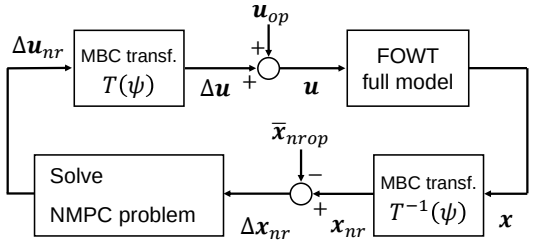

Fig. 9 Control system for NMPC based on the MBC-P model

3.3 NMPC based on the Av-P model

Next, for the Av-P model, to minimize $\boldsymbol{x} - \bar{\boldsymbol{x}}_{\mathrm{op}}$ and $\boldsymbol{y} - \bar{\boldsymbol{y}}_{\mathrm{op}}$, we define the cost functions as

$$\varphi = \frac{1}{2} \left(\boldsymbol{x} - \bar{\boldsymbol{x}}_{\mathrm{op}}\right)^{\top} Q_x \left(\boldsymbol{x} - \bar{\boldsymbol{x}}_{\mathrm{op}}\right)$$

$$L = \frac{1}{2} \left[\left(\boldsymbol{y} - \bar{\boldsymbol{y}}_{\mathrm{op}}\right)^{\top} Q_y \left(\boldsymbol{y} - \bar{\boldsymbol{y}}_{\mathrm{op}}\right) + \Delta \boldsymbol{u}^{\top} R \Delta \boldsymbol{u} \right].$$

The output for the Av-P model is given as $\boldsymbol{y} = \Delta \boldsymbol{y} + \boldsymbol{y}_{\mathrm{op}}(\psi)$. Therefore, the equilibrium $\boldsymbol{y}_{\mathrm{op}}(\psi)$ depends on ψ, and $\bar{\boldsymbol{y}}_{\mathrm{op}}$ is not canceled in $\boldsymbol{y} - \bar{\boldsymbol{y}}_{\mathrm{op}}$. Thus, this problem is NMPC because the cost functions are not quadratic, even though the state equation remains linear.

3.4 NMPCs based on the MBC-P and MBC-P-D models

Similarly, for the MBC-P and MBC-P-D models, we define the cost functions as

$$\varphi = \frac{1}{2} \left(\boldsymbol{x} - \bar{\boldsymbol{x}}_{\mathrm{op}}\right)^{\top} Q_x \left(\boldsymbol{x} - \bar{\boldsymbol{x}}_{\mathrm{op}}\right)$$

$$L = \frac{1}{2} \left[\left(\boldsymbol{y} - \bar{\boldsymbol{y}}_{\mathrm{op}}\right)^{\top} Q_y \left(\boldsymbol{y} - \bar{\boldsymbol{y}}_{\mathrm{op}}\right) + \Delta \boldsymbol{u}_{\mathrm{nr}}^{\top} R \Delta \boldsymbol{u}_{\mathrm{nr}} \right].$$

As the output is given as $\boldsymbol{y} = T_y(\psi)\left(\Delta \boldsymbol{y}_{\mathrm{nr}} + \bar{\boldsymbol{y}}_{\mathrm{nrop}}\right)$ in these models, the equilibrium $T_y(\psi)\,\bar{\boldsymbol{y}}_{\mathrm{nrop}}$ depends on ψ as it does in the Av-P model. Therefore, the cost functions are not quadratic and this problem is NMPC even though the state equations are linear.

Figures 6–9 show the closed-loop systems with the designed MPCs. In Figs. 6 and 8, the MPC optimization problems are formulated in rotating coordinates. In Figs. 7 and 9, they are formulated in nonrotating coordinates by using MBC transformation. In addition, the equilibrium is subtracted after MBC transformation in Fig. 9 and before MBC transformation in Fig. 7. This is because the dependency of the equilibrium on ψ is considered in the MBC-P model and not in the MBC-F model.

In all MPCs, we set the horizon length T to 6 s and the sampling period to 10 ms by referring to the specifications for a nacelle-mounted Doppler LIDAR wind sensor on the market [29]. Regarding the disturbance prediction, we assume that the information on the horizontal inflow wind speed can be used every 1 s, with accuracy to one decimal place [29]. We select the weighting matrices Q_x, Q_y, and R so that the platform attitude and rotor speed can be controlled as equally as possible among the five methods. Then, the differences arise primarily in the blade root bending moments, as discussed in Section 5.

4 Model Comparison

We test the accuracy of the reduced models through a numerical simulation performed using FAST on a MATLAB/Simulink platform. First, we explain the procedures and conditions for the model comparison. We linearize the full model with an interval of $\Delta\psi = 10$ [deg] and construct the reduced models as described in Section 2. Linearization is performed under steady wind conditions (16 m/s) without any wave disturbance. For comparing the fundamental characteristics of the reduced models, the steady wind is assumed to be perpendicular to the rotor plane. Then, we apply the same input as that used for the GSPI controller [4] to the five reduced models and the full model for 1000 s. That is, we control the full model by using the GSPI controller

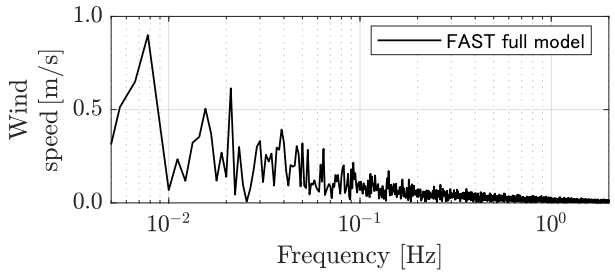

Fig. 10 Frequency responses for wind speed

and apply the time-series data of the control input to the five reduced models. The full model is tested under turbulent wind field conditions with a time step of 10 ms without wave disturbance. The mean wind speed is set to 16 m/s and the turbulence intensity is set to 12% (NTM: normal turbulence model) in accordance with the IEC design requirements [30]. Figure 10 shows the frequency response of the wind speed, whose magnitude gradually attenuates toward a high frequency. The MBC transformations and periodic equilibrium in the reduced models are calculated from the actual azimuth angle as output by the full model.

4.1 Effect of Modeling Approach on Model Accuracy

Figure 11 shows the transient responses of the five reduced models and the FAST full model. In this subsection, we compare the four reduced models (Av-F, MBC-F, Av-P, and MBC-P) by focusing on the differences in the modeling methods used. Then, we compare the MBC-P and MBC-P-D models by focusing on the effect of accounting for the inflow wind speed. As shown in Fig. 11, in terms of rotor speed and platform pitch, there are slight differences among the four reduced models (Av-F, MBC-F, Av-P, and MBC-P); in contrast, in terms of platform roll and platform yaw, there are significant differences. This indicates that the rotor speed and platform pitch do not significantly depend on the azimuth angle ψ, whereas the platform roll and platform yaw do. The platform roll and yaw are generated by the force distribution on the rotor surface, which depends on the orientation of the three blades (i.e., azimuth angle ψ). In contrast, the dynamics of the rotor speed and platform pitch are based on the total force applied on the rotor surface — which is affected by factors other than ψ, particularly the inflow wind speed.

In particular, for the platform yaw indicated in Fig. 11(e), the amplitude and frequency for the MBC-F and MBC-P models are more similar to those for the FAST full model than those for the Av-F and Av-P models. In other words, MBC transformation, in which the dependency of the perturbed dynamics on ψ is considered, is effective in modeling the platform yaw. This is because the perturbed dynamics have a more significant effect on platform yaw than the variation in the equilibrium. In fact, the Av-P model cannot reproduce the platform yaw accurately because it considers only the dependence of the equilibrium on ψ.

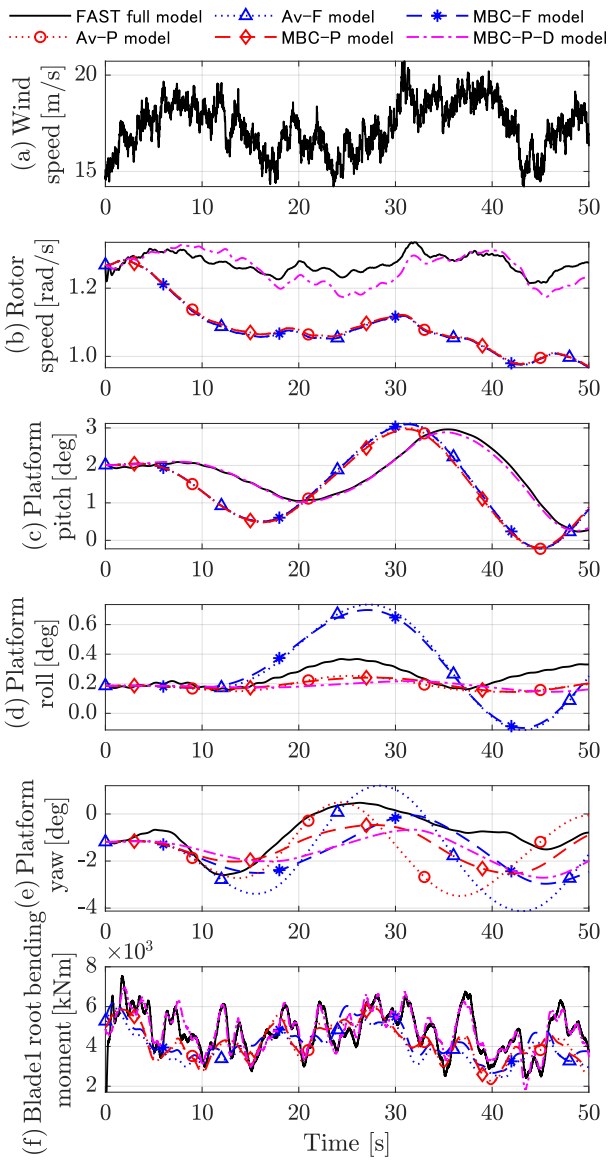

Fig. 11 Time-series data for first 50 s: (a) wind speed, (b) rotor speed, (c) platform pitch, (d) platform roll, (e) platform yaw, and (f) blade1 root bending moment

Next, we discuss the blade root bending moment by focusing on the frequency responses at 0.2 Hz, where the FAST full model exhibits a large variation. Figure 12 shows the frequency responses of blade root bending moments of the five reduced models and the FAST full model. As shown in Fig. 12, the Av-P and MBC-P models reproduce this variation at 0.2 Hz, whereas the Av-F

Table 4 Comparison of modeling approaches

Modeling approaches	Rotor speed	Platform pitch	Platform yaw	Blade root bending moment
Considering dependency of equilibrium on ψ (Av-P, MBC-P)				Good for variation around 0.2 Hz
Considering dependency of perturbed dynamics on ψ (MBC-F, MBC-P)			Good	
Considering inflow wind disturbance (MBC-P-D)	Good	Good		Good for variation over a wide frequency range

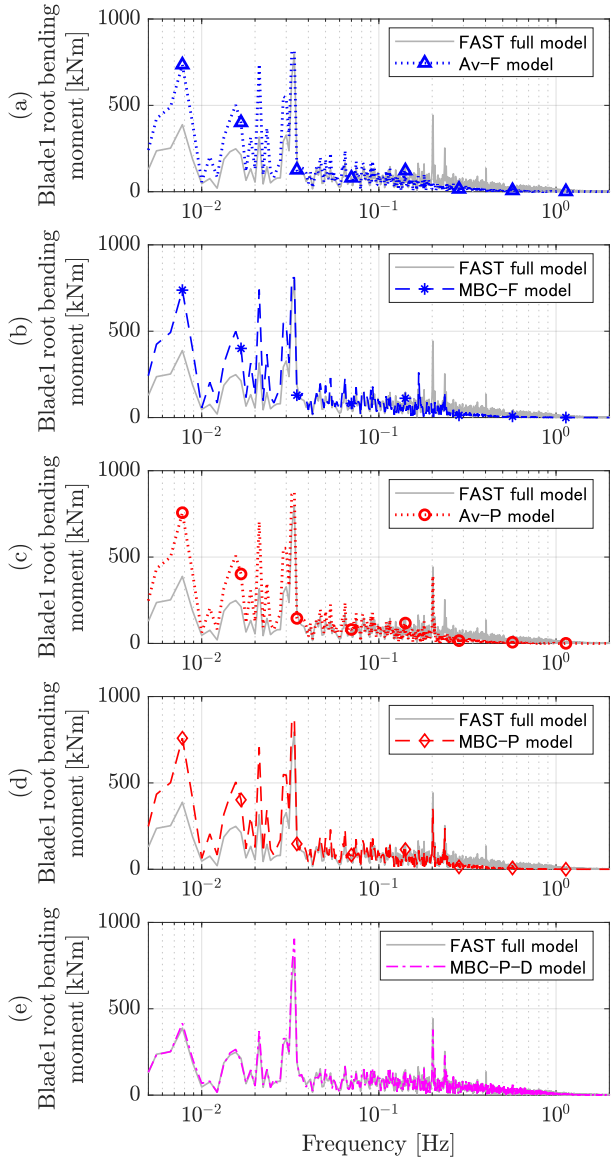

Fig. 12 Frequency responses of out-of-plane blade1 root bending moment for (a) Av-F, (b) MBC-F, (c) Av-P, (d) MBC-P, and (e) MBC-P-D models compared with that for the FAST full model

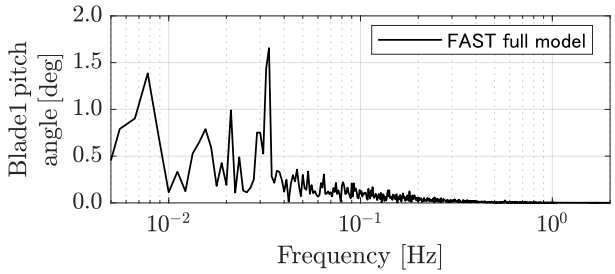

Fig. 13 Frequency responses for the blade-pitch angle, i.e., the input

and MBC-F models do not. The variation in the blade root bending moment at 0.2 Hz is caused by changes in the blade orientation, as determined by ψ. Note that 0.2 Hz corresponds to the cycle of the blade rotating at rotor speed $\dot{\psi}$ around 1.26 [rad/s]. In the Av-P and MBC-P models, the periodic equilibria, $\boldsymbol{y}_{\mathrm{op}}(\psi)$ and $T_y(\psi)\,\bar{\boldsymbol{y}}_{\mathrm{nrop}}$, reproduce this variation at 0.2 Hz. In contrast, the Av-F and MBC-F models cannot reproduce a large variation that depends on ψ, because the equilibrium is constant. In summary, by considering the periodicity of the equilibrium, the reduced models can reproduce the variation in the blade root bending moment with ψ and improve the accuracy.

4.2 Effect of Considering Inflow Wind Disturbance on Model Accuracy

In this subsection, we compare the MBC-P and MBC-P-D models by focusing on the effect of considering the inflow wind speed. As shown in Figs. 11(b) and (c), the MBC-P-D model reproduces the rotor speed and platform pitch much more accurately than the MBC-P model. That is, accounting for the inflow wind speed improves the model accuracy in terms of the rotor speed and platform pitch. This is because the dynamics of the rotor speed and platform pitch are based on the rotor torque and rotor thrust, respectively, which in turn depend on the inflow wind speed.

By contrast, there is little difference in the platform roll and platform yaw between the MBC-P and MBC-P-D models, as shown in Figs. 11(d) and (e). As the wind strikes the rotor surface mainly in the horizontal direction, the inflow wind speed does not contribute significantly to the platform roll and yaw. In addition,

the MBC-P-D model uses only the horizontal component of the inflow wind speed at the center of the rotor surface. Therefore, accounting for the wind disturbance does not make much difference for the platform roll and yaw.

Regarding the blade root bending moment, a comparison of Figs. 12(d) and (e) shows that the MBC-P-D model is more accurate than the MBC-P model over a wide frequency range. In particular, the MBC-P model does not reproduce the blade root moment of the full model in both frequency ranges below 0.04 Hz and above 0.2 Hz. This is because the MBC-P model does not account for the fluctuation in the inflow wind speed, whereas the MBC-P-D model does. In the low-frequency range, the fluctuation in the wind speed is dominant, as shown in Fig. 10, and consequently, its effect in the MBC-P-D model is not negligible. Although the fluctuation in the wind speed attenuates in the high-frequency range, it attenuates relatively slower than that in the control input, which is the blade pitch angle, as shown in Fig. 13. Therefore, it is still effective to account for the inflow wind speed even in the high-frequency range.

Table 4 summarizes the characteristics of the five reduced models observed in the simulation results. To summarize, if the information on the inflow wind speed is not available, the MBC-P model is the most accurate among the reduced models. In addition, by accounting for the inflow wind speed model, the accuracy of the MBC-P-D model is improved in terms of rotor speed, platform pitch, and blade root bending moment.

5 Controller Comparison

In this section, we discuss the performance of the controllers when implemented into the FAST full model. We test the controllers under turbulent wind field conditions with wave disturbance. The mean speed and wind turbulence intensity are set to 16 m/s and 14% (NTM), respectively, in accordance with the IEC design requirements [30]. The wave disturbance is modeled on the basis of the JONSWAP spectrum with a significant wave height of 5 m and a peak spectral period of 20 s [5, 30]. The simulations are performed for 600 s with a time step of 10 ms. The time step is set to 10 ms because a sufficiently short time step enables us to control the variation of up to 1 Hz frequencies. To prevent biased results, we use ten 600-s turbulent wind field and wave disturbance patterns.

To solve the MPC optimization problems, we use C/GMRES [31], which is a numerical algorithm for NMPC problems that enables the optimal control problem to be solved in real time. We use an automatic code generation tool AutoGenU for Maple [32,33] to generate the C code of the algorithm and integrate this code into FAST on the MATLAB/Simulink platform. In addition, we use the same algorithm for solving both LMPC and NMPC optimization problems so that they can be compared under the same conditions. We first compare the results obtained for the MPCs based on the four reduced models, which do not use the predicted wind disturbance data, and discuss the differences caused by linearization. Then, we compare the NMPCs based on the MBC-P and MBC-P-D models to evaluate the effect of using the predicted wind disturbance data.

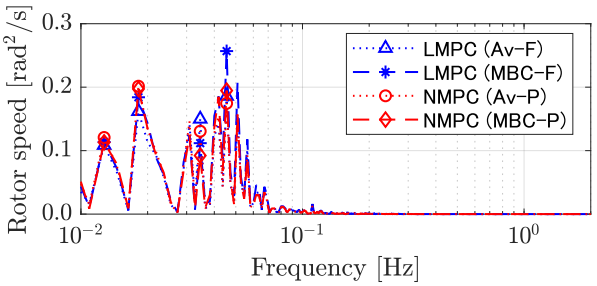

Fig. 14 Power spectral density comparison of rotor speed among four MPCs using one of the ten 600-s simulation results

Table 5 shows the RMSE with respect to each reference value, and Table 6 shows the damage equivalent load (DEL) [34], which is used for quantifying the fatigue damage in the structure. The smaller the DEL, the lesser is the fatigue damage. All values are normalized to their corresponding values for LMPC based on the Av-F model. Table 7 shows the average computation time for one update of the MPC input obtained by the simulation (Intel® Xeon® CPU E5-2667 v2 @ 3.30GHz). All RMSEs, DELs, and computation times are averaged over the 10 patterns of the simulation results.

5.1 Differences Caused by Modeling Approaches

As shown in Table 5, there are no significant differences in the rotor speed and platform pitch among the four controllers: the two LMPCs based on the conventional Av-F and MBC-F models and the two NMPCs based on the proposed Av-P and MBC-P models. Thus, it is not important whether the reduced model accounts for the dependency on ψ for controlling the rotor speed. One reason for this is that the weighting matrices are tuned such that the rotor speed and attitude are controlled equally among the four MPCs. Another reason is that the four reduced models have similar accuracies in terms of the rotor speed and platform pitch, as described in Subsection 4.1. This is evident in Fig. 14,

Table 5 Normalized root-mean-square errors of rotor speed and platform attitudes

Controller	LMPC (Av-F)	LMPC (MBC-F)	NMPC (Av-P)	NMPC (MBC-P)	NMPC#1 (MBC-P-D)	NMPC#2 (MBC-P-D)
Rotor speed	1	1.04	1.02	1.04	0.61	0.93
Platform pitch	1	1.00	1.01	1.02	1.02	0.89
Platform roll	1	1.35	0.63	1.02	0.95	0.67
Platform yaw	1	0.56	0.98	0.59	0.48	0.39
Platform surge	1	1.01	1.01	1.01	1.04	0.97

Table 6 Normalized damage equivalent load of forces and moments at blade and tower

Controller	LMPC (Av-F)	LMPC (MBC-F)	NMPC (Av-P)	NMPC (MBC-P)	NMPC#1 (MBC-P-D)	NMPC#2 (MBC-P-D)
Blade root shear force	1	0.93	0.83	0.81	0.78	0.66
Blade root bending moment	1	0.95	0.75	0.77	0.88	0.68
Tower base roll moment	1	1.20	0.67	0.92	0.91	0.65
Tower base pitch moment	1	0.96	0.97	0.94	0.99	0.92
Tower base yaw moment	1	1.54	0.81	0.92	0.93	0.75

Table 7 Computation time required for one update of control input

Controller	LMPC (Av-F)	LMPC (MBC-F)	NMPC (Av-P)	NMPC (MBC-P)	NMPC#1 (MBC-P-D)	NMPC#2 (MBC-P-D)
Computation time [ms]	0.7	0.8	0.9	1.1	1.1	1.1

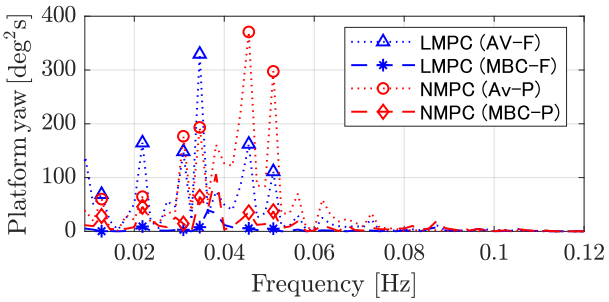

Fig. 15 PSD comparison of platform yaw between MPCs based on Av- models and those based on MBC- models using one of the ten 600-s simulation results

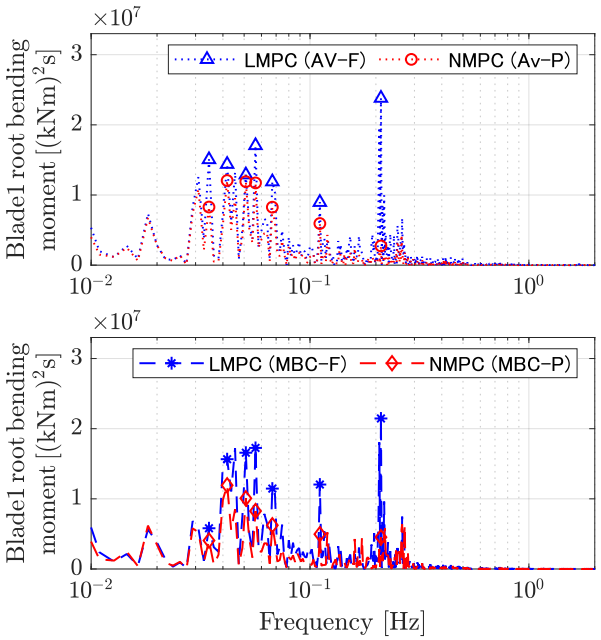

Fig. 16 PSD comparison of blade1 out-of-plane root bending moment between MPCs based on -F models and those based on -P models using one of the ten 600-s simulation results

which shows that the power spectral densities (PSDs) of the four MPCs are similar.

Table 5 shows that the MPCs based on the MBC-F and MBC-P models are highly effective in suppressing the variation in platform yaw. Figure 15 also shows that the two MPCs based on the MBC-F and MBC-P models reduce the oscillation better than those based on the Av-F and Av-P models. This is consistent with the observation in Subsection 4.1, according to which the MBC-F and MBC-P models reproduce the platform yaw in the full model more accurately than the Av-F and Av-P models.

As shown in Table 6, the NMPCs based on the Av-P and MBC-P models reduce the blade fatigue damage better than the LMPCs based on the Av-F and MBC-F models. This is mainly because the NMPCs based on the Av-P and MBC-P models take the variation in the blade moment with ψ into account, whereas the LMPCs based on the Av-F and MBC-F models do not.

This can also be observed around 0.2 Hz in Fig. 16. This is a reasonable finding given that the Av-P and MBC-P models can reproduce the blade root bending moment in the full model, whereas the Av-F and MBC-F models cannot, as discussed in Subsection 4.1.

In addition, it is also observed in Fig. 16 that the NMPCs based on the Av-P and MBC-P models reduce the variation in the blade root bending moment compared to the LMPCs based on the Av-F and MBC-F models in the frequency range of 0.04–0.08 Hz, where the fluctuation of the wave height is dominant. That is, the NMPCs based on the Av-P and MBC-P models have lower sensitivity with respect to wave disturbances than the LMPCs based on the Av-F and MBC-F models. This is again because the Av-P and MBC-P models can reproduce the blade root bending moment in the full model more accurately than the Av-F and MBC-F models.

The computation times listed in Table 7 indicate that the times for the two NMPCs are almost the same as those for the two LMPCs. This is because the state equation is linear and time-invariant even in the NMPCs, although the cost function is not quadratic. In other words, the proposed NMPCs improve the controller performance, especially in terms of the blade moment, while maintaining the computational cost sufficiently low for real-time implementation.

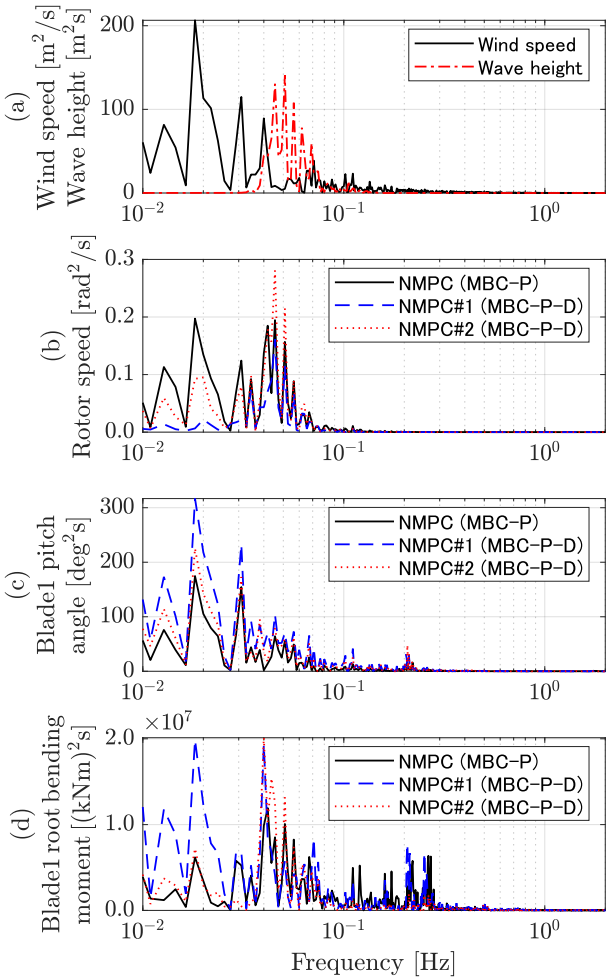

Fig. 17 PSD comparison among the three NMPCs based on the MBC-P and MBC-P-D models by using one of the ten 600-s simulation results: (a) wind speed and wave height, (b) rotor speed, (c) blade1 pitch angle, and (d) blade1 bending moment

5.2 Differences Caused by Using the Predicted Wind Disturbance Data

To verify the effect of using the predicted wind disturbance data, we evaluate two types of NMPC based on the MBC-P-D model. For NMPC#1 based on the MBC-P-D model, we use the same weighting matrices as those for NMPC based on the MBC-P model. For NMPC#2 based on the MBC-P-D model, we retune the weighting matrices by focusing more on the regulation of the attitude and blade root bending moment than on rotor speed.

Figure 17 shows PSDs in the simulations of the three NMPCs. As shown in Fig. 17(a), the fluctuation in the wind speed is dominant at frequencies below 0.04 Hz, and that of the wave height is dominant in the frequency range of 0.04–0.08 Hz. We first compare the NMPC based on the MBC-P model and NMPC#1 based on the MBC-P-D model. As shown in Table 5, NMPC#1 can effectively regulate the rotor speed by using the predicted wind disturbance data. As shown in Figs. 17(a) and (b), NMPC#1 significantly reduces the fluctuation in the rotor speed at frequencies below 0.04 Hz, compared to the NMPC based on the MBC-P model. This is because the MBC-P-D model can reproduce the rotor speed in the full model much more accurately by accounting for the inflow wind speed, as discussed in Subsection 4.2. By contrast, their responses remain almost the same from 0.04 to 0.08 Hz, where the fluctuation in the wave height is dominant. In other words, regarding the rotor speed, NMPC#1 (MBC-P-D) shows much lower sensitivity with respect to the wind speed disturbance than NMPC (MBC-P), whereas the two NMPCs show almost the same sensitivity with respect to the wave height disturbance.

Regarding the platform pitch, there is no difference between the two NMPCs, as shown in Table 5. This is because the weight of the platform pitch is less than that of the rotor speed in the weighting matrices. Thus, accounting for the inflow wind speed affects the platform pitch less than the rotor speed in the cost function of NMPC#1 based on the MBC-P-D model.

As shown in Table 6, NMPC#1 based on the MBC-P-D model does not reduce the variation in the blade root bending moment compared to the NMPC based on the MBC-P model. This is because of the trade-off between the rotor speed and blade root bending moment, which can be explained as follows. As shown in Fig. 17(c), the input of NMPC#1 fluctuates more than that of NMPC based on the MBC-P model at frequencies below 0.04 Hz in order to regulate the rotor speed. Thus, the variation in the blade root bending moment is higher at low frequencies for NMPC#1, as shown in Fig. 17(d).

Next, we compare NMPC based on the MBC-P model and NMPC#2 based on the MBC-P-D model. As shown in Tables 5 and 6, NMPC#2 reduces the RMSE and DEL for all items more than NMPC based on the MBC-P model. Compared with NMPC#1 based on the MBC-P-D model, NMPC#2 does not focus on the regulation of the rotor speed. Thus, the NMPC#2 input does not fluctuate much at low frequencies, compared with NMPC#1, as shown in Fig. 17(c). This means that NMPC#2 based on the MBC-P-D model can suppress the growth of the variation in the blade root bending moment at low frequencies, as shown in Fig. 17(d). Moreover, as shown in Fig. 17(d), NMPC#2 reduces the variation in the blade root bending moment more than that in NMPC based on the MBC-P model at frequencies above 0.1 Hz, although this cannot be acheived around 0.05 Hz. Accordingly, NMPC#2 based on the MBC-P-D model can effectively reduce the variation in the blade root bending moment at high frequencies, and consequently, the blade fatigue damage, as shown in Table 6.

Finally, as shown in Table 7, there is no difference in computation time among the three NMPCs based on the MBC-P and MBC-P-D models. The only difference between the NMPCs based on the MBC-P and MBC-P-D models is whether the wind disturbance terms are added to the state equation and cost function. In other words, even if NMPC uses the predicted wind disturbance data, the simplicity of the model is maintained, and thus, the computational cost remains low. Therefore, using the predicted wind disturbance data improves the NMPC performance while maintaining a low computational cost.

Table 8 summarizes the effectiveness of the control approaches for MPCs. In case of not using the LIDAR wind sensors, NMPC based on the MBC-P model significantly suppresses the variations in the platform yaw and blade root bending moment. In the proposed NMPC using LIDAR wind sensor data, the performance is improved, especially in regulating the rotor speed and blade root bending moment.

6 Conclusions

This paper discusses how to model and actively control FOWTs by focusing on the dependency of their dynamics on the rotor azimuth angle ψ. We proposed three new reduced models, Av-P, MBC-P, and MBC-P-D models, for controlling FOWTs by accounting for the periodicity of the equilibrium. The simulation results indicated that the proposed models reproduce the variation in the blade root bending moment more accurately than the conventional models. In particular, if information on the inflow wind speed is not available, the MBC-P model is most accurate. By accounting for the model of the inflow wind speed, the MBC-P-D model further improves the accuracy in terms of rotor speed, platform pitch, and blade root bending moment.

In addition, we proposed NMPCs minimizing the nonquadratic cost functions in accordance with the proposed models, even though the state equations in the proposed models are linear. As a result, we successfully suppressed the blade fatigue damage better than the LMPC based on the conventional models. Furthermore, although NMPC is computationally demanding and its real-time implementation is challenging, we successfully reduced the computation time required for NMPC to almost the same level as that for LMPC. In particular, if LIDAR wind sensors are not available, the NMPC based on the MBC-P model exhibits the best performance. The performance can be further improved using LIDAR wind sensors for NMPC based on the MBC-P-D model. Future work includes modeling and control of FOWTs in more complicated situations, such as a yaw misalignment between the inflow wind and platform orientation.

References

1. Musial W, Heimiller D, Beiter P, Scott G, Draxl C (2016) 2016 offshore wind energy resource assessment for the United States. NREL/TP-5000-66599. National Renewable Energy Laboratory, Golden
2. Musial W, Beiter P, Spitsen P, Nunemaker J, Gevorgian V (2019) 2018 offshore wind technologies market report. NREL/TP-5000-74278. National Renewable Energy Laboratory, Golden
3. Wright AD, Fingersh LJ (2008) Advanced control design for wind turbines; Part I: Control design, implementation, and initial tests. NREL/TP-500-42437. National Renewable Energy Laboratory, Golden
4. Jonkman J, Butterfield S, Musial W, Scott G (2009) Definition of a 5-MW reference wind turbine for offshore system development. NREL/TP-500-38060. National Renewable Energy Laboratory, Golden
5. Jonkman J (2007) Dynamics modeling and loads analysis of an offshore floating wind turbine. NREL/TP-500-41958. National Renewable Energy Laboratory, Golden

Table 8 Effectiveness of MPCs

MPC Approach	Rotor speed	Platform pitch	Platform yaw	Blade root bending moment
Use non-quadratic cost function NMPC (Av-P) and NMPC (MBC-P)				Good
Use MBC transformation LMPC (MBC-F) and NMPC (MBC-P)			Good	
Use predicted inflow wind speed data NMPC (MBC-P-D model)	Good	Good (depends on weights)	Good (depends on weights)	Good (depends on weights)

6. Robertson AN, Jonkman J (2011) Loads analysis of several offshore floating wind turbine concepts. NREL/CP-5000-50539. National Renewable Energy Laboratory, Golden
7. Shah KA, Meng F, Li Y, Nagamune R, Zhou Y, Ren Z, Jiang Z (2021) A synthesis of feasible control methods for floating offshore wind turbine system dynamics. Renewable and Sustainable Energy Reviews, 151:111525
8. Namik H, Stol K, Jonkman J (2008) State-space control of tower motion for deepwater floating offshore wind turbines. In: Proc 46th AIAA Aerospace Sciences Meeting and Exhibit, Reno, 2008–1307
9. Chaaban R, Fritzen CP (2014) Reducing blade fatigue and damping platform motions of floating wind turbines using model predictive control. In: Proc 9th International Conference on Structural Dynamics, Porto, pp 3581–3588
10. Raach S, Schlipf D, Sandner F, Matha D, Cheng PW (2014) Nonlinear model predictive control of floating wind turbines with individual pitch control. In: Proc 2014 American Control Conference, Portland, pp 4434–4439
11. Bir G (2008) Multiblade coordinate transformation and its application to wind turbine analysis. NREL/CP-500-42553, National Renewable Energy Laboratory, Golden
12. Kane MB (2020) Machine learning control for floating offshore wind turbine individual blade pitch control. In: Proc 2020 American Control Conference, Denver, pp 237–241
13. Sarkar S, Fitzgerald B, Basu B (2021) Individual blade pitch control of floating offshore wind turbines for load mitigation and power regulation. IEEE Trans Control Systems Technology, 29:305–315
14. Bagherieh O, Hedrick K, Horowitz R (2014) Nonlinear control of floating offshore wind turbines using input/output feedback linearization and sliding control. In: Proc ASME 2014 Dynamic Systems and Control Conference, San Antonio, paper no. DSCC2014-5982.
15. Navalkar ST, van Wingerden JW, Fleming PA, van Kuik GAM (2015) Integrating robust lidar-based feedforward with feedback control to enhance speed regulation of floating wind turbines. In: Proc 2015 American Control Conference, Chicago, pp 3070–3075
16. Zhao P, Nagamune R (2019) Switching LPV control of a floating offshore wind turbine on a semi-submersible platform. In: Proc 2019 IEEE 28th International Symposium on Industrial Electronics, Vancouver, pp 664-669
17. Zhang C, Tahoumi E, Gutierrez S, Plestan F, DeLeón-Morales J (2019) Adaptive robust control of floating offshore wind turbine based on sliding mode. In: Proc IEEE 58th Conference on Decision and Control, Nice, pp 6936–6941
18. Yu M, Hara N, Konishi K (2021) Blade pitch controller design based on model reference adaptive control for floating offshore wind turbines. In: Proc SICE International Symposium on Control Systems 2021, Online, 2A2-3
19. Okada Y, Haneda K, Chujo T, Ohtsuka T (2019) Parameter-varying modeling and nonlinear model predictive control for floating offshore wind turbines. In: Proc Joint Conference 8th IFAC Symposium on Mechatronic Systems and 11th IFAC Symposium on Nonlinear Control Systems, Vienna, pp 536–541
20. Schlipf D, Schuler S, Grau P, Allgöwer F, Kühn M (2010) Look-ahead cyclic pitch control using LIDAR. In: Proc Torque from Wind Third Conference, Heraklion, pp 1–7
21. Scholbrock A, Fleming P, Schlipf D, Wright A, Johnson K, Wang N (2016) Lidar-enhanced wind turbine control: past, present, and future. In: Proc 2016 American Control Conference, Boston, pp 1399–1406
22. Jonkman J, Buhl M (2005) FAST User's Guide. NREL/EL-500-38230, National Renewable Energy Laboratory, Golden
23. Browning JR, Jonkman J, Robertson A, Goupee AJ (2014) Calibration and validation of a spar-type floating offshore wind turbine model using the FAST dynamic simulation tool. J Physics: Conference Series 555:012015
24. Jain A, Robertson AN, Jonkman JM, Goupee AJ, Kimball RW, Swift AHP (2012) FAST code verification of scaling laws for DeepCwind floating wind system tests. NREL/CP-5000-54221, National Renewable Energy Laboratory, Golden
25. Ishida S, Chujo T, Haneda K, Hirao SC, Taniguchi T, Kokubun K, Inoue S (2016) Technological development and safety assessment for floating offshore wind turbines. NMRI Report, 16:107–126
26. Driscoll F, Jonkman J, Robertson A, Sirnivas S, Skaare B, Nielsen FG (2016) Validation of a FAST model of the Statoil-Hywind Demo floating wind turbine. Energy Procedia 94:3–19
27. International Renewable Energy Agency (2016) Floating foundations: a game changer for offshore wind power. `https://www.irena.org/-/media/Files/IRENA/Agency/Publication/2016/IRENA_Offshore_Wind_Floating_Foundations_2016.pdf`. Accessed: March 10, 2021
28. Utsunomiya T, Shiraishi T, Sato I, Inui E, Ishida S (2014) Floating offshore wind turbine demonstration project at Goto Islands, Japan. In: Proc OCEANS 2014 - TAIPEI, Taipei, pp 1–7
29. Mitsubishi Electric Corporation Sensing Systems Department (2018) Nacelle-mounted LIDAR. Mitsubishi Electric Corporation, Tokyo
30. International Electrotechnical Commission, IEC (2009) IEC 61400-3, Wind Turbines Part3: Design Requirements for Offshore Wind Turbines. IEC, Geneva
31. Ohtsuka T (2004) A continuation/GMRES method for fast computation of nonlinear receding horizon control. Automatica 40:563–574
32. Ohtsuka T (2015) A tutorial on C/GMRES and automatic code generation for nonlinear model predictive control. In: Proc European Control Conference, Linz, pp 73–86

33. Cybernet Systems Co. (2016) https://www.maplesoft.com/applications/view.aspx?SID=153555. Accessed: March 10, 2021
34. Freebury G, Musial W (2000) Determining equivalent damage loading for full-scale wind turbine blade fatigue tests. In: Proc 19th American Society of Mechanical Engineers Wind Energy Symposium, Reno, pp 287–296